Japanese Journal of Applied Physics **51** (2012) 016401 **REGULAR PAPER**
DOI: 10.1143/JJAP.51.016401

Calculation of Coherent Synchrotron Radiation Impedance for a Beam Moving in a Curved Trajectory

Demin Zhou[1,2*], Kazuhito Ohmi[1], Katsunobu Oide[1], Lei Zang[1], and Gennady Stupakov[3]

[1]*KEK National Laboratory, Tsukuba, Ibaraki 305-0801, Japan*
[2]*Graduate University for Advanced Studies (SOKENDAI), Hayama, Kanagawa 240-0193, Japan*
[3]*SLAC National Accelerator Laboratory, Menlo Park, CA 94025, U.S.A.*

Received May 26, 2011; revised October 4, 2011; accepted October 16, 2011; published online December 15, 2011

Coherent synchrotron radiation (CSR) fields are generated when a bunched beam moves along a curved trajectory. A new code, named CSRZ, was developed using finite difference method to calculate the longitudinal CSR impedance for a beam moving along a curved chamber. The method adopted in the code was originated by Agoh and Yokoya [Phys. Rev. ST Accel. Beams **7** (2004) 054403]. It solves the parabolic equation in the frequency domain in a curvilinear coordinate system. The chamber considered has uniform rectangular cross-section along the beam trajectory. The code was used to investigate the properties of CSR impedance of a single or a series of bending magnets. The calculation results indicate that the shielding effect due to outer chamber wall can be well explained by a simple optical approximation model at high frequencies. The CSR fields reflected by the outer wall may interfere with each other along a series of bending magnets and lead to sharp narrow peaks in the CSR impedance. In a small storage ring, such interference effect can be significant and may cause microwave instability, according to a simple estimate of instability threshold.

1. Introduction

Coherent synchrotron radiation (CSR) fields are generated when a bunched beam moves along a curved trajectory. The interests on CSR have been growing since the late 1980s when numerous dedicated synchrotron light sources were built and operated. A comprehensive historical review has been readily in hand in ref. 1. In general, CSR wakefield and CSR impedance are calculated in the time domain and frequency domain respectively. The longitudinal beam dynamics effect could then be evaluated.

CSR of an ultra-relativistic beam moving in a toroidal chamber has been studied extensively. The steady-state CSR in free space was addressed in refs. 2 and 3. The transient effect in free space was studied in ref. 4. The steady-state CSR in a rectangular toroidal chamber was also well understood.[5–7] The steady-state CSR between parallel plates has been studied by in ref. 8. For a single bending magnet with a vacuum chamber, Agoh and Yokoya[9] and Stupakov and Kotelnikov[10] have developed different frequency-domain methods to calculate the CSR impedance of a single magnet. Starting with the same wave equation, a time-domain integration method was developed in ref. 11 to calculate CSR wakefields with space-charge included. CSR fields may interfere with each other along a series of bending magnets. In such cases, one-dimensional time-domain method has also been investigated effectively in the literature.[12,13] But usually parallel plates model was used to address the shielding effect of the chamber walls.

This paper follows Agoh and Yokoya's method[9] to calculate CSR generated by a beam moving along an arbitrary trajectory. The beam trajectory could be generated by a single bending magnet (see Fig. 1), or a series of bending magnets. The relevant chamber along a series of bending magnets can be extended from Fig. 1 by adding more curved sections. At present, we assume the chamber has a uniform rectangular cross-section along the beam trajectory. To close the problem, two long straight sections are added before the entrance and after the exit of the chamber. Meanwhile, the walls of the chambers are perfectly conducting and always parallel to the beam orbit. This is essential to simplify the boundary conditions for the field equations so that the problem could be reduced to a two-dimensional one.

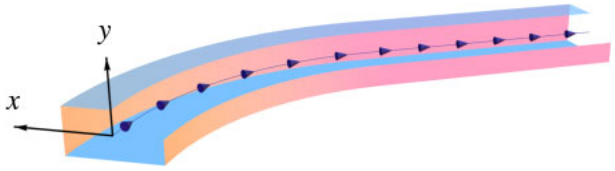

Fig. 1. (Color online) Geometry of the curved chamber for a single bending magnet. An infinitely long straight chamber is connected after the exit of the curved section. The beam moves along the curved line with arrows. The origin of the coordinate system coincides with the beam orbit.

We continue the studies presented in refs. 9 and 10 and do investigations in the following aspects: 1) the features of longitudinal CSR impedance in a single bending magnet; 2) the interference of CSR fields in a series of bending magnets and its effect on impedance. In §2, we will briefly discuss the fundamental equations for CSR theory. The numerical schemes will be described in §3. Several examples of CSR impedance calculations will be presented in §4. The CSR instability is addressed in §5. Section 6 is the summary and remarks of this work.

The method described in this paper can also be applied to calculate the CSR impedance in a wiggler or an undulator. The interested readers are referred to ref. 14.

2. Problem Statement

The fundamental equation adopted in our studies of CSR is the parabolic equation in the frequency domain in a curvilinear coordinate with the origin on the beam trajectory[9,15]

$$\frac{\partial \boldsymbol{E}_\perp}{\partial s} = \frac{i}{2k}\left[\nabla_\perp^2 \boldsymbol{E}_\perp - \frac{1}{\epsilon_0}\nabla_\perp \rho_0 + \frac{2k^2 x}{R(s)}\boldsymbol{E}_\perp\right], \qquad (1)$$

where $\boldsymbol{E}_\perp$ is the transverse electric field, and $R(s)$ is the s-dependent bending radius along the beam orbit. ϵ_0 is the vacuum permittivity. The beam is assumed to be rigid, i.e., the charge density ρ_0 does not vary along s.

*E-mail address: dmzhou@post.kek.jp

With paraxial approximation,[9] the longitudinal electric field is derived from the transverse fields and approximated as

$$E_s = \frac{i}{k}(\nabla_\perp \cdot \boldsymbol{E}_\perp - \mu_0 c J_s), \tag{2}$$

where μ_0 is the vacuum permeability, c is the speed of light in vacuum, and $J_s = \rho_0 c$ is the current density. The detailed derivations of the above equations can be found in refs. 9, 15, and 16. We will not discuss the validity of these equations either, because it has been well addressed in refs. 7 and 10.

Equation (1) also describes the field evolution in a straight chamber where the inverse bending radius is zero:

$$\frac{\partial \boldsymbol{E}_\perp}{\partial s} = \frac{i}{2k}\left(\nabla_\perp^2 \boldsymbol{E}_\perp - \frac{1}{\epsilon_0}\nabla_\perp \rho_0\right). \tag{3}$$

In our calculations, beam has a point charge form in the longitudinal direction. Then the longitudinal impedance is calculated by directly integrating E_s over s

$$Z(k) = -\frac{1}{q}\int_0^\infty E_s(x_c, y_c)\, ds \tag{4}$$

where (x_c, y_c) denotes the center of the beam in the transverse x–y plane. The appearance of the minus sign in eq. (4) is due to the convention of the beam instability formalism.

For a point charge or extremely small sizes in the transverse directions, the second term inside the brackets in eq. (1) is singular or highly peaked in the vicinity of the beam. It was found in ref. 9 that field separation approach can be adopted to smooth the field distribution. That is, to remove this singularity in numerical solution, the total field is separated into two parts: beam field in free space $\boldsymbol{E}_\perp^{\mathrm{b}}$ and radiation field $\boldsymbol{E}_\perp^{\mathrm{r}}$. For an ultra-relativistic beam, the beam field is perpendicular to the beam orbit and is independent of s. $\boldsymbol{E}_\perp^{\mathrm{b}}$ satisfies Poisson's equation as follows

$$\nabla_\perp^2 \boldsymbol{E}_\perp^{\mathrm{b}} = \frac{1}{\epsilon_0}\nabla_\perp \rho_0. \tag{5}$$

Then the evolution equation for the radiation field can be written as

$$\frac{\partial \boldsymbol{E}_\perp^{\mathrm{r}}}{\partial s} = \frac{i}{2k}\left[\nabla_\perp^2 \boldsymbol{E}_\perp^{\mathrm{r}} + \frac{2k^2 x}{R(s)}(\boldsymbol{E}_\perp^{\mathrm{r}} + \boldsymbol{E}_\perp^{\mathrm{b}})\right]. \tag{6}$$

Similarly, for the field in the straight chamber, the field evolution is approximately described by

$$\frac{\partial \boldsymbol{E}_\perp^{\mathrm{r}}}{\partial s} = \frac{i}{2k}\nabla_\perp^2 \boldsymbol{E}_\perp^{\mathrm{r}}. \tag{7}$$

We will call $\boldsymbol{E}_\perp^{\mathrm{r}}$ in a straight chamber as radiation field and will not differentiate it from the CSR field. With the assumption of ultra-relativistic beam, the beam field in free space does not contribute to the longitudinal electric field, so eq. (2) is equivalent to[9]

$$E_s = \frac{i}{k}\nabla_\perp \cdot \boldsymbol{E}_\perp^{\mathrm{r}} \tag{8}$$

Practically, in numerically calculations, the beam transverse size is assumed to be small. The distribution function is bi-Gaussian as follows

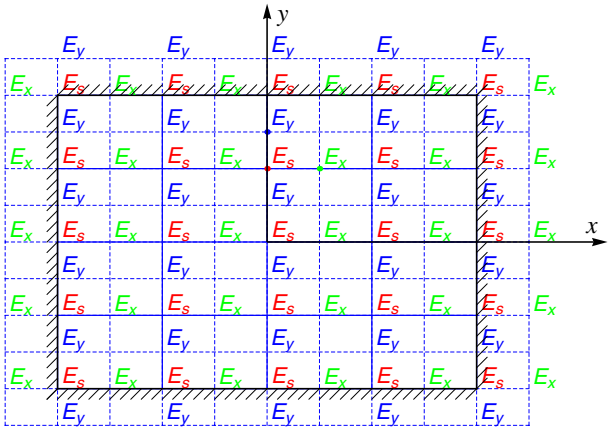

Fig. 2. (Color online) Staggered grid definition with ghost points outside the boundary of the chamber. The positions of various field components are shown. Equidistant spacing in the x and y directions is assumed. The outer all is to the right.

$$\rho_0(x, y, k) = \frac{q\lambda(k)}{2\pi c \sigma_x \sigma_y}\exp\left(-\frac{x^2}{2\sigma_x^2} - \frac{y^2}{2\sigma_y^2}\right), \tag{9}$$

where q is the total charge of the beam and $\lambda(k)$ indicates the beam spectrum in the longitudinal direction. In a typical calculation, we set $\lambda(k) = 1$, $q = 1C$, $\sigma_x = 0.1\,\mathrm{mm}$, and $\sigma_y = 0.01\,\mathrm{mm}$. With such small beam sizes, the beam field is still well concentrated in the vicinity of beam center. But it will not cause problem in numerical calculations, because the sharp peak of $\boldsymbol{E}_\perp^{\mathrm{b}}$ will be smoothed out by multiplying a small value of x in eq. (6).

3. Numerical Schemes

The numerical algorithms adopted in our work are adapted from the mesh methods originally presented in ref. 9. We start by dividing the rectangular domain $(0, a) \times (0, b)$ in the x–y plane into an equidistant $M \times N$ mesh in the x and y direction with a step size of $\Delta x = a/M$ and $\Delta y = b/N$, respectively. The mesh is shown in the solid lines in Fig. 2. The grid points in the x–y plane are given by

$$(i, j) = (i\Delta x - x_c, j\Delta y - y_c). \tag{10}$$

For any function of space and s we put

$$F^n(i, j) = F(i\Delta x - x_c, j\Delta y - y_c, n\Delta s) \tag{11}$$

where Δs indicates the step size along s.

The transverse electric fields are sampled by staggering the grid in half of a cell in both the x- and y-directions (see Fig. 2). The grid staggering provides the convenience of discretizing the field evolution equations.[9] Furthermore, it is also essential to remove the computational high-frequency modes in the finite difference formulation. The second-order derivative is calculated by applying central finite difference approximation and the derivative with respect to s is approximated by the leapfrog difference. The leapfrog algorithm is fully explicit and conditionally stable. Unconditionally stable implicit schemes are available[17–19] and have the advantages of allowing for large step size Δs. However, they are usually more complicated to program. For example, in each solution step the matrix inversions will be involved, which required more computational efforts.

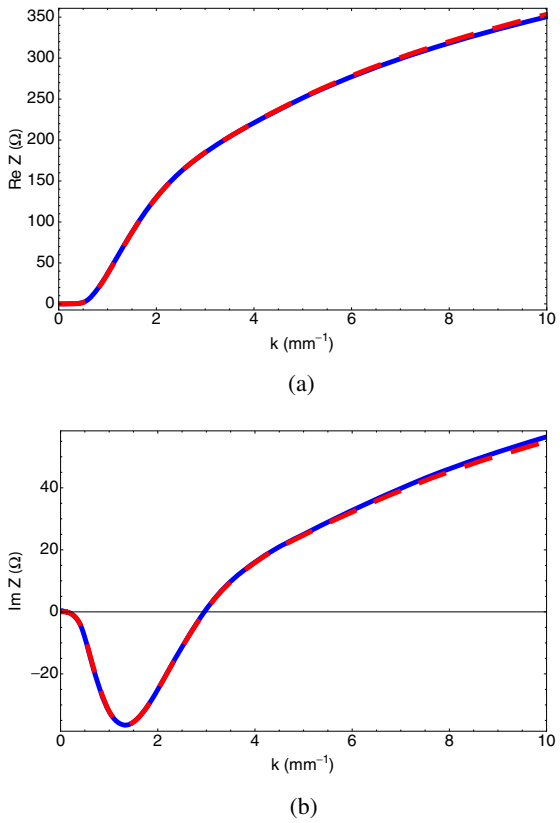

Fig. 3. (Color online) CSR impedance for a single bending magnet with $R = 1\,\mathrm{m}$ and $L_\mathrm{b} = 0.2\,\mathrm{m}$ for (a) real part and (b) imaginary part. The dimensions of the chamber cross-section are $a = 6\,\mathrm{cm}$, and $b = 2\,\mathrm{cm}$. The blue solid and red dashed lines are given by Stupakov's code and the code CSRZ, respectively.

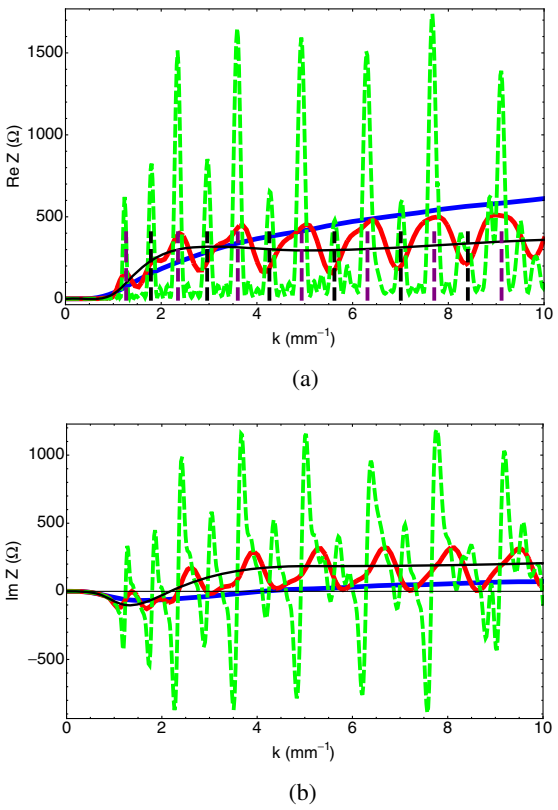

Fig. 4. (Color online) CSR impedance for a single bending magnet with $R = 5\,\mathrm{m}$ and varied length of the curved chamber $L_\mathrm{b} = 0.5, 2, 8\,\mathrm{m}$ for (a) real part and (b) imaginary part. The dimensions of the chamber cross-section are $a = 6\,\mathrm{cm}$, and $b = 3\,\mathrm{cm}$. The impedances have been normalized by the length of the curved chamber. Blue solid lines: $L_\mathrm{b} = 0.5\,\mathrm{m}$; red solid lines: $L_\mathrm{b} = 2\,\mathrm{m}$; green dashed lines: $L_\mathrm{b} = 8\,\mathrm{m}$; black solid lines: parallel plates model. The purple and black dashed lines denote E_x and E_y modes with $p = 1$, respectively.

The grid in the x–y plane, as shown in Fig. 2, does not vary along s due to the assumption of uniform chamber cross-section. The second-order central finite difference requires additional ghost points which are half cell outside the chamber wall surfaces. The equivalent finite-difference equations for the evolution equations and the boundary conditions will be skipped in this paper. For the details, readers are referred to refs. 9, 14, and 16.

4. Numerical Results

The methods discussed in §2 and §3 are implemented in a new code named CSRZ using the programming language FORTRAN 90 on a workstation. In this section, we will present a few examples of using this code. Through this section, the beam is always located at the center of the chamber in the x–y plane, i.e., $(x_\mathrm{c}, y_\mathrm{c}) = (a/2, b/2)$.

4.1 Single bending magnet

We start to calculate the longitudinal CSR impedance of a single short bending magnet with constant bending radius in a curved chamber. The magnet parameters are chosen as the same as Fig. 9 in ref. 10: the bending radius $R = 1\,\mathrm{m}$, and the length of the curved chamber $L_\mathrm{b} = 0.2\,\mathrm{m}$. The horizontal and vertical dimensions of the chamber's cross-section are $a = 6\,\mathrm{cm}$ and $b = 2\,\mathrm{cm}$, respectively. The calculation results were compared with those given by Stupakov's code[10] (see Fig. 3). The comparison shows a good agreement in general. The tiny discrepancy in the high frequency impedance is due to the mesh sizes we chose in calculation. Decreasing the mesh sizes, resulting in longer computer time, can give better results which are converged to those given by the mode expansion method.[10] Thus, the benchmark between two independent methods confirmed the capability of the new code CSRZ.

The previous example shows smooth CSR impedance for a short magnet. In the next example, we investigate the influence of the length of the curved chamber. At this time, we choose $R = 5\,\mathrm{m}$, $a = 6\,\mathrm{cm}$, and $b = 3\,\mathrm{cm}$ and vary the curved chamber length as $L_\mathrm{b} = 0.5, 2, 8\,\mathrm{m}$. The impedance results are shown in Figs. 4(a) and 4(b). In the same figures, we also plot the results given by the parallel plates model.[9] And the corresponding wake potentials with a short bunch of rms length $\sigma_z = 0.5\,\mathrm{mm}$ are given in Fig. 5. When $L_\mathrm{b} = 0.5\,\mathrm{m}$, which indicates a short curved chamber, the impedance is very smooth. When the curved chamber gets longer, the impedance becomes fluctuating with an interval of around $1.3\,\mathrm{mm}^{-1}$ in wavenumber and eventually results in a series of resonant peaks. This observation clearly indicates that the CSR impedance is actually correlated to the eigenmodes of the curved chamber.[15] When the curved chamber is long enough, some specific modes which fulfill the phase matching condition can be strongly excited by the beam and become dominant in the radiation fields.

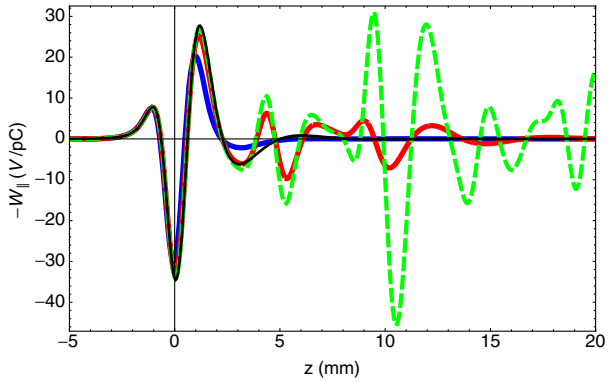

Fig. 5. (Color online) Short-bunch wake potentials due to CSR in a single bending magnet with $R = 5$ m and varied length of the curved chamber $L_b = 0.5, 2, 8$ m. The dimensions of the chamber cross-section are $a = 6$ cm, and $b = 3$ cm. The gaussian bunch length $\sigma_z = 0.5$ mm with bunch head to the left side. The wake potentials have been normalized by the length of the curved chamber. Blue solid lines: $L_b = 0.5$ m; red solid lines: $L_b = 2$ m; green dashed lines: $L_b = 8$ m; black solid lines: parallel plates model.

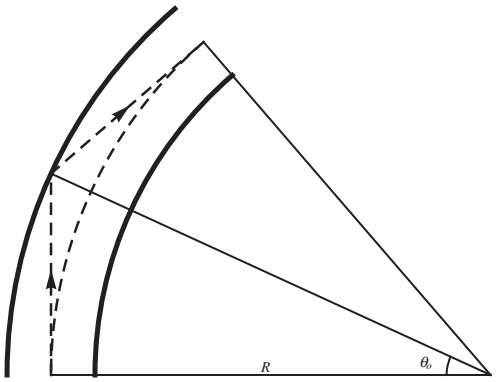

Fig. 6. CSR reflected by the outer wall of the beam pipe. The beam starts to radiate fields at the entrance of the curved chamber. The dashed curve without arrows on it denotes the beam orbit. The arrowed dashed lines represent the direction of the radiation fields.

One can compare the wavenumbers at the resonant peaks in Fig. 4 with the analytical predictions shown in refs. 6, 7, and 15. According to ref. 7, the resonant peaks should appear at wavenumbers

$$k_{mp} = \frac{p\pi}{b}\sqrt{\frac{R}{x_o}}\Upsilon\left(\frac{b(m \pm 0.25)}{px_o}\right), \tag{12}$$

where the integer indices m and p denote the individual mode of the curved chamber and x_o is the distance from the beam to the outer wall in the horizontal plane. The plus sign in eq. (12) indicates E_x modes in which $E_y = 0$ and $m = 0, 1, 2, 3, \ldots$; the minus sign indicates E_y modes in which $E_x = 0$ and $m = 1, 2, 3, \ldots$. p must be odd numbers, i.e., $p = 1, 3, 5, \ldots$. Finally, $\Upsilon(r)$ is defined by

$$\Upsilon(r) = \left[\left(\sqrt{1+\frac{r^2}{3}}+1\right)^{1/3} - \left(\sqrt{1+\frac{r^2}{3}}-1\right)^{1/3}\right]^{-3/2}. \tag{13}$$

When r is large, $\Upsilon(r)$ can be approximated by $3r/2^{3/2}$.[7] It infers that the resonance peaks in the CSR impedance are almost equally spaced along the wavenumber axis. The resonances are indicated by vertical dashed lines in Fig. 4. They agree well with the observed peaks from numerical calculations.

As stated in refs. 7 and 10, when the aspect ratio of the curved chamber a/b is larger than 2, the shielding of the inner and outer walls can be neglected and the parallel plates model is a good approximation for a long bending magnet. This criteria works well in the low frequency region with $k < k_{th}$ as proved in ref. 7. Here k_{th} is the shield threshold defined by[7]

$$k_{th} = \pi\sqrt{\frac{R}{b^3}}. \tag{14}$$

Our calculations do agree with this criteria as depicted in Fig. 4. On the contrary, in the high frequency region, the CSR impedance significantly differs from the parallel plates model and exhibits fluctuations and even narrow resonance peaks for a long curved chamber. A geometrical explanation for this observation was proposed in ref. 20 as illustrated in Fig. 6. CSR field is radiated in the direction almost tangent to the beam trajectory when a beam enters the curved chamber. The outer wall plays a role of mirror and reflects the field back to the beam. If the curved chamber is long enough, the reflected fields can accumulate and become significant. The geometrical picture of CSR suggests a critical length of

$$L_o = 2R\theta_o \approx 2\sqrt{2Rx_o} \tag{15}$$

for the curved chamber. Here $\theta_o = \arccos[R/(R + x_o)] \approx \sqrt{2x_o/R}$, and the approximation is justified when the chamber dimension is much smaller than the bending radius, i.e., $x_o \ll R$. If $L_b \gg L_o$, some specific modes can be strongly excited and results in the fluctuations or resonant peaks in the CSR impedance. If $L_b \leq L_o$, such fluctuations will be negligible. But if $L_b \ll L_o$, transient effect will also become important. The critical length indicates a length when the reflection of the outer wall becomes important. But L_o does not depends on the aspect ratio of the pipe cross-section. Therefore, the condition of neglecting shielding due to the outer wall, i.e., $L_b \leq L_o$, can be a supplement for $k > k_{th}$.

Similar to the optical approximation in the theory of geometric impedance,[21] the critical length L_o defined by eq. (15) can also be interpreted as a catch-up distance over which the CSR, generated by the head of a beam, reflects from the outer wall and reaches the beam tail at length Δs_o behind the head. It is easy to calculate Δs_o from the geometry shown in Fig. 6, and the result is[20]

$$\Delta s_o = 2R(\tan\theta_o - \theta_o) \approx \frac{4}{3}\sqrt{\frac{2x_o^3}{R}}. \tag{16}$$

The quantity Δs_o corresponds to a modulation wavenumber of[20]

$$\Delta k = \frac{2\pi}{\Delta s_o} \approx \frac{3\pi}{2}\sqrt{\frac{R}{2x_o^3}}. \tag{17}$$

It turns out that $\Delta k = k_{(m+1)p} - k_{mp}$ is exactly the distance between adjacent resonances for the same vertical index p and large argument r in eq. (13). When comparing Δs_o with

the bunch length σ_z, one can find the condition of neglecting outer-wall shielding effect in evaluating CSR induced instability, i.e., $\Delta s_o \gg \sigma_z$. Namely, this condition says that the reflected CSR fields from the outer wall can never catch up with the beam tail and thus has no influence on the beam in total.

One can check eqs. (16) and (17) by applying them to the examples depicted in Fig. 4(a). The value $\Delta k = 1.4\,\mathrm{mm}^{-1}$ is close to the observed value of $1.3\,\mathrm{mm}^{-1}$. $\Delta s_o = 4.4\,\mathrm{mm}$ is roughly the distance at which the first peak appears in the tail part of the wake potential in Fig. 5. Since the bunch length $\sigma_z = 0.5\,\mathrm{mm}$ is much smaller than Δs_o, the amplitude of the wake potential in the vicinity of the beam is almost independent of magnet length. Thus, we can conclude that the outer-wall shielding mainly impose effects in the tail part of CSR wake.

As depicted in Fig. 6, the radiation fields take a longer path than the beam. Thus, the previous discussions on outer-wall shielding holds for the trailing fields. A similar geometric interpretation holds for the shielding of overtaking fields due to the inner chamber wall. Detailed discussions are given in ref. 22. The relevant critical length of the curved chamber is

$$L_i = 2R\theta_i \approx 2\sqrt{2Rx_i}, \tag{18}$$

with $\theta_i = \arccos[(R - x_i)/R] \approx \sqrt{2x_i/R}$. The quantity x_i is the distance from the beam to the inner wall in the horizontal plane, and the approximations are justified if $x_i \ll R$. When the beam travels the distance of L_i, the radiation fields will overtake the head of the beam at

$$\Delta s_i = 2R(\theta_i - \sin\theta_i) \approx \frac{2}{3}\sqrt{\frac{2x_i^3}{R}}. \tag{19}$$

If $\Delta s_i \gg \sigma_z$, one can expect that the overtaking fields will reach the bunch head without seeing the inner chamber wall. Thus, the shielding due to the inner wall will be negligible. On the other hand, if $\Delta s_i < \sigma_z$, the inner-wall shielding should be taken into account.

In summary, the shielding effects of the outer and inner walls can be treated separately: the trailing fields reflect at the outer wall, resulting in a head-to-tail interaction; the overtaking fields may be shielded by the inner wall, affecting the well-known tail-to-head interaction. In a storage ring, it is usually true that the beam centroid coincides with the center of the vacuum chamber. In this case, we will have $x_o = x_i = a/2$, $L_o = L_i$, and $\Delta s_i = \Delta s_o/2$. It turns out that the condition of neglecting chamber-wall shielding can be approximated as $\sigma_z \ll \sqrt{a^3/R}$. This is exactly the condition found in ref. 22.

4.2 Interference in a series of bending magnets

In a realistic storage ring, the bending magnets are arranged consecutively along the beam orbit. There is a concern that interference may enhance CSR fields generated in a series of bending magnets. Our code can treat this case straightforwardly. As an example, we place four identical hard-edge magnets along s. The drift chambers between the 4 magnets are also identical. In this case, $R^{-1}(s)$ can be described by a step function. The parameters for the magnets and chamber are $R = 5\,\mathrm{m}$, $L_b = 2\,\mathrm{m}$, $a = 6\,\mathrm{cm}$ and $b = 3\,\mathrm{cm}$. The length of the drift chambers is $L_d = 2\,\mathrm{m}$. The impedance is plotted

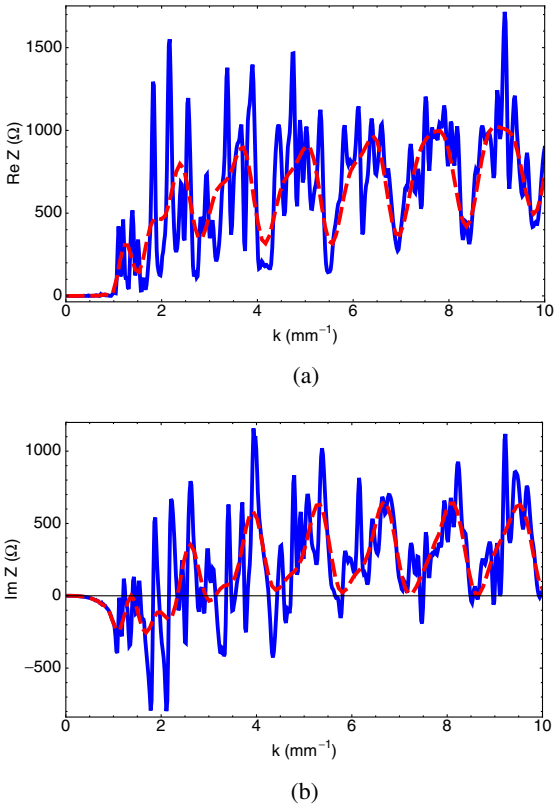

Fig. 7. (Color online) CSR impedance for four bending magnets interleaved with equidistant drift chambers for (a) real part and (b) imaginary part. The magnet parameters: $R = 5\,\mathrm{m}$, $L_b = 2\,\mathrm{m}$. The length of drift chamber: $L_d = 2\,\mathrm{m}$. The dimensions of the chamber cross-section: $a = 6\,\mathrm{cm}$, $b = 3\,\mathrm{cm}$. The blue and dashed red lines are the impedances with and without considering interference, respectively.

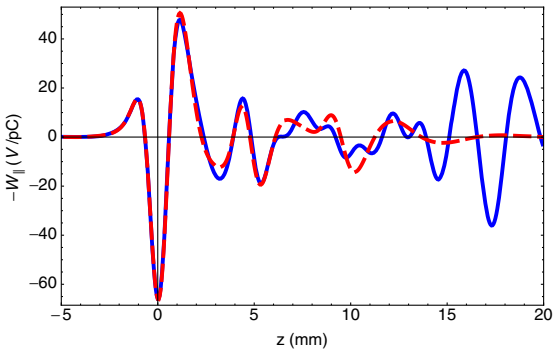

Fig. 8. (Color online) Short-bunch wake potentials due to CSR in four bending magnets interleaved with equidistant drift chambers. The magnet parameters: $R = 5\,\mathrm{m}$, $L_b = 2\,\mathrm{m}$. The length of drift chamber: $L_d = 2\,\mathrm{m}$. The dimensions of the chamber cross-section are $a = 6\,\mathrm{cm}$, and $b = 3\,\mathrm{cm}$. The gaussian bunch length $\sigma_z = 0.5\,\mathrm{mm}$ with bunch head to the left side. The wake potentials have been normalized by the number of magnets.

in Figs. 7(a) and 7(b) and compared with that of single magnets. The corresponding wake potentials with a short bunch of rms length $\sigma_z = 0.5\,\mathrm{mm}$ are given in Fig. 8. One sees that the impedance spectrum contains a forest of peaks, which indicate that specific eigenmodes can satisfy the phase matching conditions and will be excited by the beam. The impedance of a single magnet looks to be

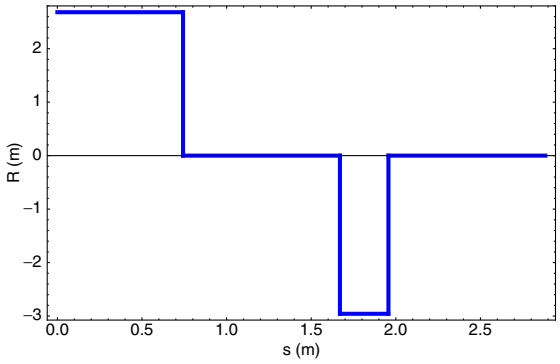

Fig. 9. (Color online) Bending radius as a function of s for one cell in the arc sections of SuperKEKB positron damping ring.

broad-band approximation of that of a series of magnets. The narrow spikes in the impedance lead to long-range wake fields far behind the bunch as seen in the wake potential.

Naturally one can suspect that if there are many bending magnets placed in a long curved chamber, many high peaks may exists in the CSR impedance. This is proved by a more practical case of the SuperKEKB positron damping ring. In the SuperKEKB damping ring,[23] there are two arc sections. In each section, there are in total 16 cells. Each cell contain two reverse bending magnets,[24] of which the bending radius as a function of s is shown in Fig. 9. The drift between consecutive cells is around 1 m. The vacuum chamber cross-section is approximated by a square with $a = b = 3.4$ cm. The CSR impedances of one arc section (in total 16 cells), of 6 consecutive cells, and of 1 cell are calculated. The results are compared with that of single-bend model as shown in Figs. 10(a) and 10(b). It is not surprising that many narrow and high peaks appear in the impedance spectrum when the number of cells grows. And the CSR impedance calculated using single magnet model again provides a broad-band approximation. The wake potentials with rms bunch length of 0.5 mm corresponding to the previous impedances are plotted in Fig. 11. The figure clearly shows that the tail parts are strongly modulated due to interference effect. We also observed that the shape of wake potential due to 6 cells is already close to that of 16 cells at the distance less than 20 mm to the beam center. This is because that the CSR fields generated at the first cells keeps far behind the beam and almost are damped out in the range considered after the beam traverses several arc cells.

5. Microwave Instability Threshold Due to CSR

As shown in Fig. 10, in a practical ring like SuperKEKB positron damping ring, CSR impedance including interference effect contains sharp narrow peaks. The peaks indicates field resonances generated by consecutive bending magnets. There is concern that if such resonant CSR impedance is considered, beam will become unstable. The threshold of microwave instability due to CSR can be estimated by solving the dispersion relation[25,26] or by solving Vlasov–Fokker–Planck equation.[27] For a simple instability analysis, one can apply the Keil–Schnell criterion[28] to a bunched beam[29]

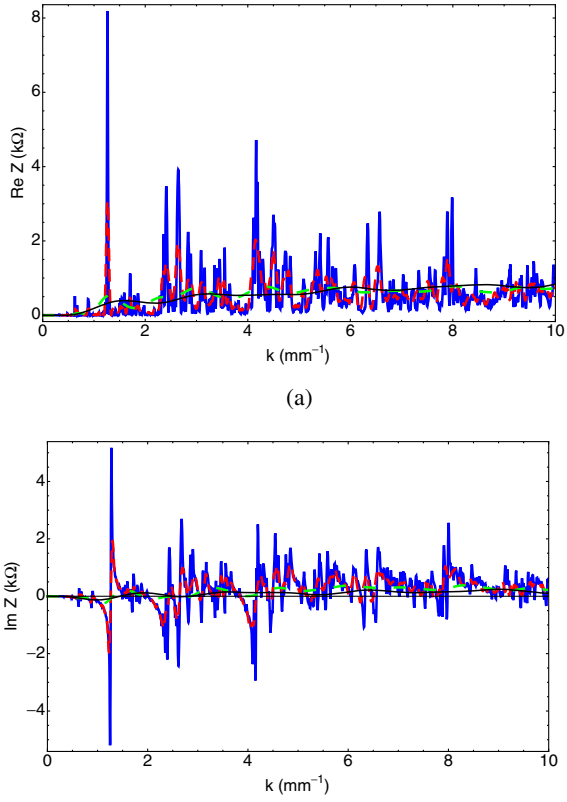

Fig. 10. (Color online) CSR impedance of the arc section in the SuperKEKB positron damping ring for (a) real part and (b) imaginary part. The impedances have been normalized by the number of cells for convenience of comparision. Blue solid line: 16 cells; red dashed line: 6 cells; Green dashed line: 1 cell; Black solid line: single-bend model.

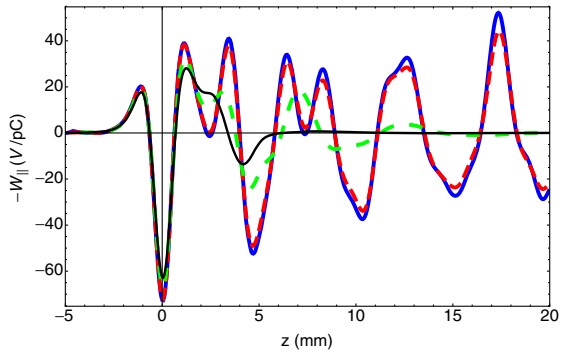

Fig. 11. (Color online) Short-bunch wake potentials due to CSR in the arc section of SuperKEKB positron damping ring. The gaussian bunch length $\sigma_z = 0.5$ mm with bunch head to the left side. The wake potentials have been normalized by the number of cells. Blue solid line: 16 cells; red dashed line: 6 cells; Green dashed line: 1 cell; Black solid line: single-bend model.

$$\left|\frac{Z_{\parallel}}{n}\right| < FZ_0 \frac{\gamma \alpha_p \sigma_\delta^2 \sigma_z}{N_0 r_e}, \tag{20}$$

where $Z_{\parallel}/n$ is the longitudinal impedance driving the instability, α_p is the momentum compaction factor, σ_δ is the relative energy spread, σ_z is the rms bunch length, N_0 is the bunch population, r_e is the classical radius of electron. F

is a form factor, for a gaussian bunch, we take it as $F = \sqrt{\pi/2}$. $n = \omega/\omega_0$ is the harmonic and ω_0 is the revolution angular frequency. The above equation is also called Keil–Schnell–Boussard criterion. It is apparent that this criterion can only provide a crude estimate of the instability threshold in a storage ring. As pointed out in ref. 30, this criterion is only correct for a broad-band impedance wider than the frequency spectrum of the bunch. In principle, sharp resonances can also drive microwave instabilities.[31] But, as derived from ref. 30, it is more appropriate to use a modified criterion as follows:

$$\left|\frac{\sqrt{2\pi}k_0\sigma_z}{4}\frac{R_s}{Q}\right| < FZ_0\frac{\gamma\alpha_p\sigma_\delta^2\sigma_z}{N_0 r_e}, \tag{21}$$

to detect the instability threshold driven by sharp resonances, of which the frequency width is much narrower than that of bunch spectrum. In the above equation, $k_0 = \omega_0/c = 2\pi/C$ where C is the circumference of the storage ring. One should notice that eq. (21) is written in the form that it has the same right side as eq. (20). In the above equation, R_s is shunt impedance, Q is quality factor and k_r is the resonant impedance. These parameters define the well-known resonator impedance model of

$$Z_\parallel(k) = \frac{R_s}{1 + iQ(k_r/k - k/k_r)}. \tag{22}$$

As an example, let us examine the resonant peak at $k_r = 1.264\,\mathrm{mm}^{-1}$ in the CSR impedance shown in Fig. 10. This peak is close to the first mode defined by eq. (12) and exhibits large amplitude and relatively large width. As shown in the figure, R_s and Q should be functions of number of cells N_{cell}. We fit this peak using eq. (22) and get the corresponding parameters of R_s and Q. The results are plotted in Fig. 12. The figures show that the quality factor is almost a linear function of N_{cell}. And $R_s/Q/N_{\mathrm{cell}}$ converges to a constant of around $130\,\Omega$ when $N_{\mathrm{cell}} > 5$, this agree with the shape of calculated wake potentials in Fig. 11. Larger values are observed at $N_{\mathrm{cell}} < 5$ and we believe it is due to fitting errors. It is seen that for small number of cells, the CSR impedance spectrum becomes broad-band and neighboring resonant peaks overlap with each other.

Next we check the instability threshold using a set of machine parameters of SuperKEKB positron damping ring as shown in ref. 23. The parameters are listed as follows: $C = 135.5\,\mathrm{m}$, $\gamma = 2153$, $\alpha_p = 0.0141$, $\sigma_\delta = 5.5 \times 10^{-4}$, $\sigma_z = 7.74\,\mathrm{mm}$, $N_0 = 5.0 \times 10^{10}$. Using these parameters, the right hand side of eq. (21) is calculated to be $0.24\,\Omega$.

The bunch length of $\sigma_z = 7.74\,\mathrm{mm}$ corresponds to a critical bandwidth $0.13\,\mathrm{mm}^{-1}$ in unit of wavenumber. With $k_r = 1.264\,\mathrm{mm}^{-1}$, the critical quality factor is $Q_{\mathrm{th}} = 9.8$. Comparing with Fig. 12(a), we conclude that when $N_{\mathrm{cell}} > 5$, eq. (21) should be applied. Choosing $R_s/Q/N_{\mathrm{cell}} = 130\,\Omega$ and taking into account the total number of cells $N_{\mathrm{cell}} = 32$ for two arc sections, we obtain an impedance of $0.95\,\Omega$ for the left hand side of eq. (21). This value is quite above $0.24\,\Omega$ which is defined by machine parameters. It implies that CSR may be of importance in the SuperKEKB positron damping ring. More careful studies via standard numerical simulations, which is beyond the scope of this paper, should be done to estimate the threshold with CSR included.

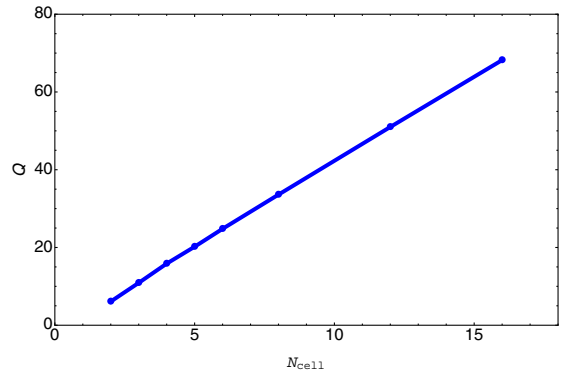

(a)

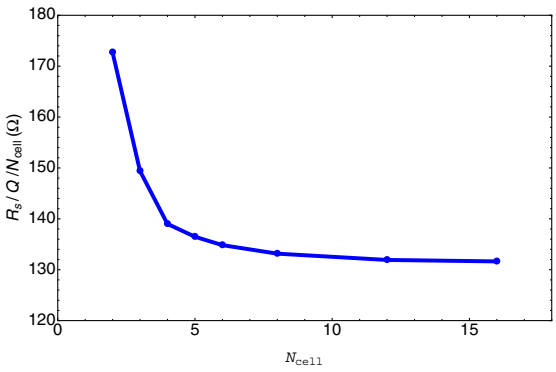

(b)

Fig. 12. (Color online) Quality factor (a) and shunt impedance (b) as a function of number of cells at the resonant peak of $k_r = 1.264\,\mathrm{mm}^{-1}$. CSR impedances are calculated using different number of cells in one arc section of SuperKEKB positron damping ring dipole magnents. The shunt impedances have been normalized by the number of cells and quality factor.

6. Summary and Remarks

In this paper we presented the numerical calculations of the longitudinal CSR impedance for a beam moving in an arbitrarily curved chamber. The CSRZ code was used to investigate the properties of CSR impedance of a single bending magnet. It turns out that the magnet length, in addition to the chamber aspect ratio, may also play an important role in defining the profile of CSR impedance and wake function. For a long magnet, the shielding effect of the outer wall can be well understood using a geometric model. With this code, the interference among CSR fields in a series of bending magnets could be approached. The calculations revealed that the interference can be significant in a small storage ring. In such a ring, the bending radius may be in the order of a few meters, and the CSR fields reflected by the outer wall may reach the bunch tail if the bunch length is in the order of a few millimeters. Our studies suggested that during evaluating the CSR instabilities in a small storage ring, interference effect should be taken into account.

Acknowledgments

The author DZ wish to acknowledge Y. Cai (SLAC) for helpful discussions and also the support for DZ's several trips to SLAC. Fruitful discussions with T. Agoh, K. Yokoya, M. Kikuchi, and H. Ikeda are deeply appreciated.

1) J. Murphy: Beam Dyn. Newsl. **35** (2004) 20.
2) B. G. Schinov, A. G. Bonch-Osmolovski, V. G. Makhankov, and V. N. Tsytovitch: Plasma Phys. **15** (1973) 211.
3) A. Faltens and L. J. Laslett: Part. Accel. **4** (1973) 151.
4) E. L. Saldin, E. A. Schneidmiller, and M. V. Yurkov: Nucl. Instrum. Methods Phys. Res., Sect. A **490** (2002) 1.
5) K.-Y. Ng: Part. Accel. **25** (1990) 153.
6) R. L. Warnock and P. Morton: Part. Accel. **25** (1990) 113.
7) T. Agoh: Phys. Rev. ST Accel. Beams **12** (2009) 094402.
8) J. B. Murphy, S. Krinsky, and R. L. Gluckstern: Part. Accel. **57** (1997) 9.
9) T. Agoh and K. Yokoya: Phys. Rev. ST Accel. Beams **7** (2004) 054403.
10) G. V. Stupakov and I. A. Kotelnikov: Phys. Rev. ST Accel. Beams **12** (2009) 104401.
11) D. R. Gillingham and T. M. Antonsen: Phys. Rev. ST Accel. Beams **10** (2007) 054402.
12) C. Mayes and G. Hoffstaetter: Phys. Rev. ST Accel. Beams **12** (2009) 024401.
13) D. Sagan, G. Hoffstaetter, C. Mayes, and U. Sae-Ueng: Phys. Rev. ST Accel. Beams **12** (2009) 040703.
14) D. Zhou: Ph. D. thesis, The Graduate Univsersity for Advanced Studies (2011).
15) G. V. Stupakov and I. A. Kotelnikov: Phys. Rev. ST Accel. Beams **6** (2003) 034401.
16) T. Agoh: Ph. D. thesis, University of Tokyo (2004).
17) F. Zhen, Z. Chen, and J. Zhang: IEEE Trans. Microwave Theory Tech. **48** (2000) 1550.
18) F. Zheng and Z. Chen: IEEE Trans. Microwave Theory Tech. **49** (2001) 1006.
19) I. Ahmed, E.-K. Chua, E.-P. Li, and Z. Chen: IEEE Trans. Antennas Propag. **56** (2008) 3596.
20) K. Oide: presented at Mini CSR Workshop, KEK, 2010.
21) G. Stupakov, K. L. F. Bane, and I. Zagorodnov: Phys. Rev. ST Accel. Beams **10** (2007) 054401.
22) Y. S. Derbenev, J. Rossbach, E. L. Saldin, and V. D. Shiltsev: Tech. Rep. TESLA FEL-Rep. 1995-05 (1995).
23) M. Kikuchi, T. Abe, K. Egawa, H. Fukuma, K. Furukawa, N. Iida, H. Ikeda, T. Kamitani, K. Kanazawa, K. Ohmi, K. Oide, K. Shibata, M. Tawada, M. Tobiyama, and D. Zhou: Proc. 1st Int. Particle Accelerator Conf., 2010, p. 1641.
24) M. Kikuchi: Nucl. Instrum. Methods Phys. Res., Sect. A **556** (2006) 13.
25) G. Stupakov and S. Heifets: Phys. Rev. ST Accel. Beams **5** (2002) 054402.
26) S. Heifets and G. Stupakov: Phys. Rev. ST Accel. Beams **6** (2003) 064401.
27) K. L. F. Bane, Y. Cai, and G. Stupakov: Phys. Rev. ST Accel. Beams **13** (2010) 104402.
28) E. Keil and W. Schnell: Tech. Rep. CERN Rep. No. CERN-ISR-TH-RF/69-48 (1969).
29) D. Boussard: Tech. Rep. CERN Lab II/RF/Int./75-2 (1975).
30) K. Ng: Proc. Summer Study on Physics of SSC, 1986, p. 590.
31) J. E. Griffin and J. A. MacLachlan: IEEE Trans. Nucl. Sci. **32** (1985) 2359.